

## Causality guided machine learning model on wetland $\text{CH}_4$ emissions across global wetlands

Kunxiagia Yuan<sup>a</sup>, Qing Zhu<sup>a\*</sup>, Fa Li<sup>a,c</sup>, William J. Riley<sup>a</sup>, Margaret Tom<sup>a</sup>, Hause Chu<sup>a</sup>, Gavin McNicol<sup>b</sup>, Min Chen<sup>c</sup>, Sara Knox<sup>d</sup>, Kyle Delwiche<sup>e</sup>, Huayi Wu<sup>f</sup>, Dennis Baldocchi<sup>e</sup>, Hongyu Ma<sup>g</sup>, Ankur R. Desai<sup>h</sup>, Jiquan Chen<sup>i</sup>, Torsten Sachs<sup>j</sup>, Masahito Ueyama<sup>k</sup>, Oliver Sonnenstag<sup>l</sup>, Manuel Helbig<sup>m</sup>, Eeva-Stiina Tuutila<sup>n</sup>, Gerald Jurasinski<sup>o</sup>, Franziska Koebisch<sup>p</sup>, David Campbell<sup>q</sup>, Hans Peter Schmid<sup>r</sup>, Annalea Lohila<sup>s</sup>, Mathias Goedkede<sup>t</sup>, Mats B. Nilsson<sup>u</sup>, Thomas Friberg<sup>v</sup>, Joachim Jansen<sup>w</sup>, Donatella Zona<sup>x</sup>, Eugenie Euskirchen<sup>y</sup>, Eric J. Ward<sup>z</sup>, Gil Bohrer<sup>aa</sup>, Zhenong Jin<sup>ab</sup>, Licheng Liu<sup>ab</sup>, Hiroki Iwata<sup>ac</sup>, Jordan Goodrich<sup>q</sup>, Robert Jackson<sup>ad</sup>

<sup>a</sup> Climate and Ecosystem Sciences Division, Climate Sciences Department, Lawrence Berkeley National Laboratory, Berkeley, CA, USA

<sup>b</sup> Department of Earth and Environmental Sciences, University of Illinois at Chicago, Chicago, IL, USA

<sup>c</sup> Department of Forest and Wildlife Ecology, University of Wisconsin-Madison, Madison, WI, USA

<sup>d</sup> Department of Geography, The University of British Columbia, Vancouver, British Columbia, Canada

<sup>e</sup> Department of Environmental Science, Policy, and Management, University of California, Berkeley, CA, USA

<sup>f</sup> State Key Laboratory of Information Engineering in Surveying, Mapping and Remote Sensing, Wuhan University, Wuhan, China

<sup>g</sup> Department of Geography, University of California, Berkeley, CA, USA

<sup>h</sup> Department of Atmospheric and Oceanic Sciences, University of Wisconsin-Madison, Madison, WI, USA

<sup>i</sup> Department of Geography, Environment, and Spatial Sciences, Michigan State University, East Lansing, MI, USA

<sup>j</sup> GFZ German Research Centre for Geosciences, Potsdam, Germany

<sup>k</sup> Graduate School of Life and Environmental Sciences, Osaka Prefecture University, Sakai, Japan

<sup>l</sup> Département de Géographie, Université de Montréal, Montréal, QC, Canada

<sup>m</sup> Department of Physics and Atmospheric Science, Dalhousie University, Halifax, NS, Canada

<sup>n</sup> School of Forest Sciences, University of Eastern Finland, Joensuu, Finland

<sup>o</sup> Landscape Ecology, University of Rostock, Rostock, Germany

<sup>p</sup> Digital Forest, University of Göttingen, Göttingen, Germany

<sup>q</sup> School of Science, University of Waikato, Hamilton, New Zealand

<sup>r</sup> Karlsruhe Institute of Technology, Institute of Meteorology and Climate Research, Karlsruhe, Germany

<sup>s</sup> Institute for Atmospheric and Earth System Research/Forest Sciences, University of Helsinki, Helsinki, Finland

<sup>t</sup> Department of Biogeochemical Signals Max Planck Institute for Biogeochemistry, Jena, Germany

<sup>u</sup> Department of Forest Ecology and Management, Swedish University of Agricultural Sciences, Umeå, Sweden

<sup>v</sup> Department of Geosciences and Natural Resource Management, University of Copenhagen, Copenhagen K, Denmark

<sup>w</sup> Department of Ecology and Genetics, Uppsala University, Uppsala, Sweden

<sup>x</sup> Department of Biology, San Diego State University, San Diego, CA, USA

<sup>y</sup> Institute of Arctic Biology, University of Alaska Fairbanks, Fairbanks, AK, USA

<sup>z</sup> U.S. Geological Survey, Wetland and Aquatic Research Center, Lafayette, LA, USA

<sup>aa</sup> Department of Civil, Environmental & Geodetic Engineering, Ohio State University, Columbus, OH, USA

<sup>ab</sup> Department of Bioproducts and Biosystems Engineering, University of Minnesota, St Paul, MN, USA

<sup>ac</sup> Department of Environmental Science, Faculty of Science, Shinshu University, Matsumoto, Japan

<sup>ad</sup> Department of Earth System Science, Stanford University, Stanford, CA, USA

### ARTICLE INFO

#### Keywords

Eddy covariance  $\text{CH}_4$  emission

Wetlands

### ABSTRACT

Wetland  $\text{CH}_4$  emissions are among the most uncertain components of the global  $\text{CH}_4$  budget. The complex nature of wetland  $\text{CH}_4$  processes makes it challenging to identify causal relationships for improving our understanding and predictability of  $\text{CH}_4$  emissions. In this study, we used the flux measurements of  $\text{CH}_4$  from eddy covariance

\* Corresponding author.

E-mail address: [qzhu@lbl.gov](mailto:qzhu@lbl.gov) (Q. Zhu).

towers (30 sites from 4 wetland types: bog, fen, marsh, and wet tundra) to construct a causality-constrained machine learning (ML) framework to explain the regulatory factors and to capture  $\text{CH}_4$  emissions at sub-seasonal scale. We found that soil temperature is the dominant factor for  $\text{CH}_4$  emissions in all studied wetland types. Ecosystem respiration ( $\text{CO}_2$ ) and gross primary productivity exert controls at bog, fen, and marsh sites with lagged responses of days to weeks. Integrating these asynchronous environmental and biological causal relationships in predictive models significantly improved model performance. More importantly, modeled  $\text{CH}_4$  emissions differed by up to a factor of 4 under a  $+1^\circ\text{C}$  warming scenario when causality constraints were considered. These results highlight the significant role of causality in modeling wetland  $\text{CH}_4$  emissions especially under future warming conditions, while traditional data-driven ML models may reproduce observations for the wrong reasons. Our proposed causality-guided model could benefit predictive modeling, large-scale upscaling, data gap-filling, and surrogate modeling of wetland  $\text{CH}_4$  emissions within earth system land models.

## 1. Introduction

Methane ( $\text{CH}_4$ ) has been the second most important contributor to post-industrial global warming after carbon dioxide ( $\text{CO}_2$ ), with a Global Warming Potential (GWP) of 28–34 times of  $\text{CO}_2$  over a 100-year time horizon (Bergamaschi et al., 2013; IPCC, 2013). Wetland  $\text{CH}_4$  emissions are the largest natural global sources, contributing around 20–30% to global emissions (Bousquet et al., 2006; Chen and Prinn, 2006; Saundis et al., 2020). Global warming (Koff et al., 2020), anthropogenic emissions (Boothroyd et al., 2017), wetland expansion (Zhang et al., 2017), and increasing methanogenic substrate availability (Schuur et al., 2008) are expected to increase  $\text{CH}_4$  emissions and thereby amplify climate warming (Tao et al., 2020). Freshwater wetlands remain the largest and most uncertain natural  $\text{CH}_4$  source to the atmosphere (Peltola et al., 2019; Saundis et al., 2020), but with considerable discrepancies among bottom-up biogeochemistry models, top-down atmospheric inversion models, and data-driven machine learning models (Koff et al., 2020; Peltola et al., 2019; Saundis et al., 2020). Therefore, improvements in the understanding of uncertainty sources and development of robust modeling frameworks for  $\text{CH}_4$  emissions are required to estimate present-day and future wetland  $\text{CH}_4$  emissions (Dean et al., 2018).

Wetland  $\text{CH}_4$  emissions are affected by multiple environmental (e.g., temperature, redox conditions) and biological (e.g., plant photosynthesis, microbial enzyme activity) factors (Delwiche et al., 2021; Knox et al., 2021). Wetland  $\text{CH}_4$  is produced by methanogens under anaerobic conditions (Mayer and Conrad, 1990), with the production rate controlled by multiple drivers such as temperature, availability of substrate (Bergman et al., 2000; Schaefer et al., 2010; Whalen, 2005),  $\text{O}_2$  and alternative electron acceptors (Pasut et al., 2021). After production,  $\text{CH}_4$  can be emitted to the atmosphere through various pathways (e.g., diffusion, ebullition, plant aerenchyma transport) that are affected by temperature, water depth, air pressure, and plant aerenchyma properties (Bastviken, 2009; Knox et al., 2021; Morin et al., 2014; Rey-Sánchez et al., 2018; Villa et al., 2020).  $\text{CH}_4$  can be oxidized by aerobic bacteria when passing through oxic soil or water during transport (Whalen, 1993) or even via anaerobic pathways (anaerobic oxidation of methane, AOM) (Fan et al., 2021). The impacts of environmental and biological factors on  $\text{CH}_4$  emissions are often non-linear and operate over a range of timescales (Sturtevant et al., 2016). For example, the response of  $\text{CH}_4$  production to temperature is observed to be hysteretic (Chang et al., 2021) due to seasonal substrate availability and microbial activity (Chang et al., 2020). The response of  $\text{CH}_4$  emissions to GPP may be delayed and the relationship between them has been observed to be lagged by hours to days (Hatala et al., 2012a; Rime et al., 2018), while  $\text{CH}_4$  emission responses to water table fluctuations can be lagged by days to months (Chen et al., 2021; Goodrich et al., 2015; Sturtevant et al., 2016). The multi-driver dependency, nonlinearity, and time-lagged characteristics make it challenging to understand how  $\text{CH}_4$  emissions interact with environmental and biological factors and to accurately represent them in predictive models (Kimet et al., 2020; Sturtevant et al., 2016; Turner et al., 2021).

In most ecosystem biogeochemical models, wetland  $\text{CH}_4$  production is represented as a function of net primary production and/or

heterotrophic respiration (as a proxy for microbial activity), with both constrained by environmental scalars (Milton et al., 2013; Wania et al., 2013; Xu et al., 2016). For example, temperature sensitivity scalars have been proposed based on observed  $\text{CH}_4$  emissions (Yvon-Durocher et al., 2014). However, in situ observations reveal high variability and uncertainty in  $\text{CH}_4$  emissions even with nearly identical environmental conditions (Chadburn et al., 2020; Granberget et al., 1997; Hemes et al., 2018; Koch et al., 2014; Rime et al., 2018; Villa et al., 2021; Zona et al., 2016), implying much more complex functional relationships between  $\text{CH}_4$  emissions and environmental and biological factors. A few ecosystem models explicitly represent more of the underlying microbial, plant, and abiotic processes leading to wetland  $\text{CH}_4$  emissions (e.g., ecosys (Grant et al., 2015; Grant et al., 2017a; Grant et al., 2017b), BAM54 (Pasut et al., 2021), and JSBACH-methane (Castro-Morales et al., 2018)) and confirm that these nonlinear interactions should be considered to improve model predictions of methane emissions (Chang et al., 2019).

In addition to the ecosystem biogeochemical models, Machine Learning (ML) models are becoming useful tools for capturing complex nonlinear relationships, and have achieved good performance in gap filling  $\text{CH}_4$  emission data (Hatala et al., 2012a; Hatala et al., 2012b; Ivin et al., 2021; Kim et al., 2020; Knox et al., 2019; Morin et al., 2014) and spatial upscaling (Peltola et al., 2019). However, widely-applied ML frameworks do not accurately represent lagged  $\text{CH}_4$  emission dependencies (Kim et al., 2020). Including lagged variables as predictors may improve ML model performance, but risks overfitting especially for multiple-driver dominated ecosystems with limited temporal observations (Kim et al., 2020). Furthermore, commonly used ML models do not consider causality constraints (Pearl, 2019; Reichstein et al., 2019). Such ML models may fit an observational dataset well while not being driven by causal relationships (Pearl, 2019; Runge et al., 2019a). In this study, we explore whether an ML model that represents lagged responses and considers underlying causal relationships can improve process understanding and wetland  $\text{CH}_4$  emission predictions.

We used  $\text{CH}_4$  emission measurements at 30 eddy covariance towers covering 4 wetland types (bog, fen, marsh, and wet tundra), to test three hypotheses: (1) It is possible to infer with statistical confidence causal relationships between drivers and  $\text{CH}_4$  emissions. (2) The environmental drivers significantly affecting methane emissions differ among the wetlands by their type and location. (3) Future model predictions that are well calibrated based on current flux observations but differ in their assumed causal relationships between drivers and methane emissions will diverge significantly. To test these hypotheses, we develop an integrated framework that combines causality and ML to improve understanding of causal relationships affecting  $\text{CH}_4$  emissions and modeling of wetland  $\text{CH}_4$  emissions across various wetland ecosystems. In this work, a causal relationship exists between predictor ( $X$ ) and  $\text{CH}_4$  emissions if, when excluding the confounding effects from other predictors and from the history of  $\text{CH}_4$  emissions, knowing the predictor ( $X$ ) could significantly reduce the uncertainty in predicting  $\text{CH}_4$  emissions (Abdul Razak and Jensen, 2014; Runge et al., 2019a). The overarching goal of this study is to develop, train, and validate a ML model to improve predictive modeling of wetland  $\text{CH}_4$  emission for diverse wetlands.

## 2 Methodology

### 2.1. Study sites and data description

The dataset used in this study is from the FLUXNET-CH<sub>4</sub> synthesis activity, which compiles, standardizes, and gap-fills available daily eddy covariance CH<sub>4</sub> emission data, via the regional networks of AmeriFlux, EuroFlux, OzFlux, and AsiaFlux (Delwiche et al., 2021; Knox et al., 2019). We focus on four types of natural freshwater wetlands (bog, fen, marsh, and wet tundra), and use 30 wetland sites, each with at least one year of CH<sub>4</sub> observations (Fig. 1; Table 1). The wetland classification is based on the site-specific literature (Delwiche et al., 2021). Daily CH<sub>4</sub> emissions (F<sub>CH<sub>4</sub></sub>) and 13 potential drivers are considered in our analysis: Air Temperature (T<sub>a</sub>), Topsoil Temperature (T<sub>s</sub>) (detailed information of soil temperature depth can be seen in Delwiche et al. (2021)), Water Table Depth (D<sub>W</sub>), Precipitation (P), Soil Water Content (θ), Relative Humidity (RH), Vapor Pressure Deficit (VPD), Atmospheric Pressure (PA), Wind Speed (WS), and Incoming Shortwave Radiation (SW); and biological factors Gross Primary Production (GPP), Ecosystem Respiration (RECO), and Net Ecosystem Exchange (NEE) (See variable availability for each site in Table S1). These variables are widely acknowledged as important driving factors for wetland CH<sub>4</sub> emissions (Knox et al., 2021; Oertel et al., 2016). Details of data standardization for the FLUXNET-CH<sub>4</sub> dataset are presented in Knox et al. (2019). In this study, we used the observed non-gap-filled measurements to maintain the original dynamic patterns and avoid potential biases from the gap-filling algorithms that have their own assumed causal relationships.

### 2.2 Transfer entropy analysis

We employ a transfer entropy approach with PCMI framework (Runge et al., 2019b) to identify non-linear directional relationships between environmental and biological factors and F<sub>CH<sub>4</sub></sub>. Transfer entropy is a powerful tool to reveal the causality for non-linear and asynchronous systems (Bouskill et al., 2020; Liu et al., 2019; Schreiber, 2000). The approach quantifies information entropy flow from source variables (e.g., T<sub>a</sub>) to the target variable (F<sub>CH<sub>4</sub></sub>) by measuring the information entropy reduction in the target variables when excluding effects from various confounders (Yuan et al., 2022; Li et al., 2022). If transfer entropy is statistically significant, the causal relationship from a source variable to the target variable is confirmed. For each pair of variables of interest, we calculate the transfer entropy (T) from source variable X to target variable Y considering the confounders of Z (Schreiber, 2000):

$$T(X \rightarrow Y) = \sum_{y_t, z, x_t^{[l]}} p(y_t, z, x_t^{[l]}) \log_2 \frac{p(y_t | (z, x_t^{[l]}))}{p(y_t | z)} \quad (1)$$

where l is the corresponding time lag of source variable X. p is the probability density. Compared with the linear and nonlinear correlation based methods (e.g., mutual information in Knox et al. (2021)), transfer entropy can explicitly exclude confounding effects when detecting the causal strength from one variable to F<sub>CH<sub>4</sub></sub> through removing shared information between confounders (Z) and the target variable (Y).

In theory, all potential confounders should be included when identifying causal relationships. However, in practice, too many confounders will cause high dimensionality and statistical instability issues (Runge et al., 2019b; Yuan et al., 2021). For simplicity, previous studies often considered the immediate history of a target variable as the confounder, assuming that it contributes the most confounding information to the target (Ruddell and Kumar, 2009; Yuan et al., 2021). However, wetland F<sub>CH<sub>4</sub></sub> can be jointly regulated by multiple factors including the history of F<sub>CH<sub>4</sub></sub>. To minimize the interferences from important confounders and to avoid high dimensionality, we adaptively considered three confounders that have the strongest control on the variation of F<sub>CH<sub>4</sub></sub> through the PCMI framework (Runge et al., 2019b). PCMI contains two key steps (1) PC (named after its inventors Peter and Clark) (Spirtes et al., 2000) and (2) Momentary Conditional Independence (MCI) (Runge et al., 2019b). To infer the causal strength from a source variable to the target variable, we firstly used the transfer entropy method in PC to rank the contribution of all potential confounders (e.g., air temperature, soil water content) with relative lower dimensionality (Spirtes et al., 2000), and used transfer entropy in MCI to calculate the causal strength from a source variable to the target variable by excluding the information entropy from the most important confounders (Runge et al., 2019b). We iteratively conducted the causal inference process for each variable to obtain the causal strength (Fig. S1).

The shuffled surrogate method (Kantz and Schüermann, 1996) was employed to test the statistical significance of transfer entropy. This method randomly shuffles source and target time series to destroy time correlations. Shuffled surrogate transfer entropy was computed 100 times through Monte Carlo simulations. A one-tailed significance test is then applied to determine the 95% confidence of the transfer entropy (Ruddell and Kumar, 2009).

### 2.3 CH<sub>4</sub> emission predictive models

We develop a causality constrained interpretable ML model based on the Long-Short-Term-Memory framework (Guo et al., 2019a; Hochreiter and Schmidhuber, 1997; Li et al., 2020) for prediction (hereafter causal-LSTM). We compared the causal-LSTM model performance, internal functional relationships, and model sensitivity against its baseline LSTM model (described below), to illustrate the benefit of including causality constraints in prediction.

#### 2.3.1. Baseline model

The baseline naïve LSTM model has been widely used in time sequence predictions (Alahi et al., 2016; Li et al., 2020). One of the advanced features of LSTM is the gate mechanism that controls the information flow to be memorized or forgotten, which enables capturing short-term and long-term dependencies underlying data sequences. Here, we use the LSTM model for prediction, given the lagged responses of emissions to environmental and biological factors. The recursive representations of LSTM and prediction can be represented as

$$\begin{aligned} h_t, c_t &= f(x_t, h_{t-1}, c_{t-1}) \\ \hat{Y}_{T+1} &= W h_T + b_l \end{aligned} \quad (2)$$

where x<sub>t</sub> (t is timestep, 0 < t ≤ T) is the input vector, q is the cell memory state vector, and h<sub>t</sub> represents the hidden state vector with useful

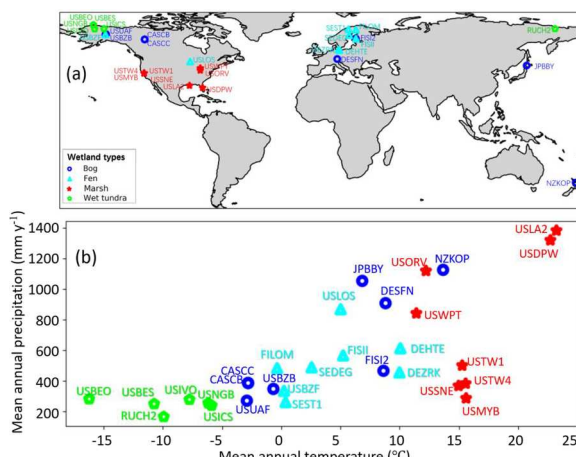


Fig. 1. (a) Geographic locations and wetland types of the 30 selected eddy covariance sites. (b) Mean annual temperature and precipitation of each site.

**Table 1**  
FLUXNET-CH<sub>4</sub> site information of the 30 sites used in this analysis

Wetland Type	Site ID	Site name	IGBP	LAT	LON	Startyear	Endyear	Data DOI	References
Bog	CA-SCB	Scotty Creek Bog	WET	61	-121	2014	2017	DOI: 10.18140/FLX/1669613	(Sonnenstag and Helbig, 2020a)
	CA-SOC	Scotty Creek Landscape	ENF	61	-121	2013	2016	DOI: 10.18140/FLX/1669628	(Sonnenstag and Helbig, 2020b)
	DE-SIN	Schechenif Iz Nord	WET	48	11.33	2012	2014	DOI: 10.18140/FLX/1669635	(Schmid and Klatt, 2020)
	FI-Si2	Siikaneva II	WET	62	24.2	2012	2016	DOI: 10.18140/FLX/1669639	(Vesila et al., 2020)
	JP-BB1	Bibai bog	WET	43	141.8	2015	2018	DOI: 10.18140/FLX/1669646	(Ueyama et al., 2020)
	NZ-Kop	Koputai	WET	-37	175.6	2012	2015	DOI: 10.18140/FLX/1669652	(Campbell and Goodrich, 2020)
	US-BZB	Bonanza Creek Thermokarst Bog	WET	65	-148	2014	2016	DOI: 10.18140/FLX/1669668	(Euskirchen and Edgar, 2020a)
	US-Uaf	University of Alaska, Fairbanks	ENF	65	-148	2011	2018	DOI: 10.18140/FLX/1669701	(Wata et al., 2020)
	DE-Hte	Huetelmoor/Rodenwiese	WET	54	12.18	2011	2018	DOI: 10.18140/FLX/1669634	(Koebisch and Jurasiczki, 2020)
	DE-Zrk	Zamekow	WET	54	12.89	2013	2018	DOI: 10.18140/FLX/1669636	(Sachs and Wille, 2020)
Fen	FI-Lom	Lompolojärkkä	WET	68	24.21	2006	2010	DOI: 10.18140/FLX/1669638	(Lohila et al., 2020)
	FI-Si	Siikaneva I (FI-Si)	WET	62	24.19	2013	2018	DOI: 10.18140/FLX/1669640	(Vesila et al., 2020)
	SE-Deg	Degro	WET	64	19.56	2014	2018	DOI: 10.18140/FLX/1669659	(Nilsson and Reichl, 2020)
	SE-Si1	Stordalen Mire	WET	65	19.05	2012	2014	DOI: 10.18140/FLX/1669660	(Jansen et al., 2020)
	US-BZF	Bonanza Creek Rich Fen	WET	65	-148	2014	2016	DOI: 10.18140/FLX/1669669	(Euskirchen and Edgar, 2020b)
	US-Los	Lost Creek	WET	46	-90	2014	2018	DOI: 10.18140/FLX/1669682	(Desai and Thom, 2020)
	US-DPW	Disney Wilderness Preserve Wetland	WET	28	-81.4	2013	2017	DOI: 10.18140/FLX/1669672	(Hinkle and Bracho, 2020)
Marsh	US-LA2	Salvador WMA Freshwater Marsh	WET	30	-90.3	2011	2013	DOI: 10.18140/FLX/1669681	(Högl et al., 2020)
	US-Mb	Mayberry Wetland	WET	30	-122	2011	2018	DOI: 10.18140/FLX/1669685	(Matthes et al., 2020)
	US-Orv	Clentangy River Wetland Research Park	WET	40	-83	2011	2015	DOI: 10.18140/FLX/1669689	(Bohrer and Mohr, 2020)
	US-Sne	Sherman Island Restored Wetland	GRA	38	-122	2016	2018	DOI: 10.18140/FLX/1669693	(Shortt et al., 2020)
	US-Tw1	Twitchell Wetland West Pond	WET	38	-122	2011	2018	DOI: 10.18140/FLX/1669696	(Valach et al., 2020)
	US-Tw4	Twitchell East End Wetland	WET	38	-122	2013	2018	DOI: 10.18140/FLX/1669698	(Eichelmann et al., 2020)
	US-WPT	Winoos Point North Marsh	WET	41	-83	2011	2013	DOI: 10.18140/FLX/1669702	(Chen and Chu, 2020)
	RU-Ch2	Chersky Reference	WET	69	161.4	2014	2016	DOI: 10.18140/FLX/1669654	(Godeke, 2020; Godeke et al., 2019)
	US-Beo	Barrow Environmental Observatory (BEO) tower	WET	71	-157	2013	2014	DOI: 10.18140/FLX/1669664	(Zona and Oechel, 2020a)
	US-Bes	Barrow-Bes (Biotic Complexity Experiment South tower)	WET	71	-157	2013	2015	DOI: 10.18140/FLX/1669665	(Zona and Oechel, 2020b)
Wet tundra	US-Ics	Irmavait Creek Watershed Wet Sedge Tundra	WET	69	-149	2014	2016	DOI: 10.18140/FLX/1669678	(Euskirchen et al., 2020)
	US-Ivo	Ivotuk	WET	68	-156	2013	2016	DOI: 10.18140/FLX/1669679	(Zona and Oechel, 2020)
	US-NGB	NGEE Arctic Barrow	SNO	71	-157	2012	2018	DOI: 10.18140/FLX/1669687	(Torn and Dengel, 2020)

information for predictions. In this study,  $x_t$  represents the biotic and abiotic drivers across sites;  $h_t$  is the hidden state vector at the last time step T;  $\hat{Y}_{T+1}$  is the predicted  $F_{CH_4}$  at the time step T+1; and  $W$  and  $b$  are the parameters that need to be learned. The  $f$  in Eq. (2) is an integrated function that includes five individual equations

$$\begin{aligned}
 f_t &= \sigma(W_{xf}x_t + W_{hf}h_{t-1} + b_f) \\
 i_t &= \sigma(W_{xi}x_t + W_{hi}h_{t-1} + b_i) \\
 o_t &= \sigma(W_{xo}x_t + W_{ho}h_{t-1} + b_o) \\
 c_t &= f_t \odot c_{t-1} + i_t \odot \tanh(W_{xc}x_t + W_{hc}h_{t-1} + b_c) \\
 h_t &= o_t \odot \tanh(c_t)
 \end{aligned} \tag{3}$$

where  $f_t$ ,  $i_t$ , and  $o_t$  are gating vectors that control how much information for the cell memory to forget, input/update, and output, respectively;  $\sigma$  is the sigmoid activation function;  $\odot$  is element-wise product;  $W_{xf}$ ,  $W_{hf}$ ,  $W_{xi}$ ,  $W_{hi}$ ,  $W_{xo}$ ,  $W_{ho}$ ,  $W_{xc}$ , and  $W_{hc}$  are linear transformation matrices that need to be learned; and  $b_f$ ,  $b_i$ ,  $b_o$ ,  $b_c$ , and  $b_t$  are corresponding bias vectors obtained through model training.

For the LSTM, we used the recursive feature elimination (RFE) method (Guyon et al., 2002) to remove spurious predictors. Specifically, we iteratively removed one predictor, used the remained predictors to train the LSTM, and calculated the correlation coefficient between

observations and predictions after removing the predictor. Then, we removed the weakest predictor which showed the lowest impacts on model performance, and repeated the predictor elimination process until only one predictor was left. Finally, we present LSTM modeling results based on the subset of predictors selected by RFE method that have the highest model performance.

### 2.3.2 Causality constrained LSTM

Although baseline LSTM is capable of capturing short-term and long-term dependencies in the input time series, it works as a black-box and cannot explicitly select important driving variables and lacks interpretability of its predictions. Also, the dependencies identified within the LSTM model are based on correlations rather than causality (a more informative directional relationship). To this end, the LSTM model can be improved through attention mechanism, an effective weight assignment method, to increase its transparency (Alahi et al., 2016; Guo et al., 2019a; Li et al., 2020; Li et al., 2017; Li et al., 2018; Li et al., 2017; Vasavada et al., 2017). The weight mechanism explicitly and dynamically assigns larger weights to more important variables, thereby improving model performance and interpretability (Guo et al., 2019a; Li et al., 2020). However, without the guide or constraint of causality, the correlation-based ML models may represent wrong processes (e.g., miscapture dominant causal drivers) (Mbraffah et al., 2020; Pearl, 2019; Runge et al., 2019b), making the model unreliable, especially for predictions using multiple drivers with similar seasonal trends (confounding) information under climate change (Runge et al., 2019a). In addition, we further imposed additional constraints using causal relationships from input variables to the target variable and led to the causal-LSTM model. The causal-LSTM model first calculated the causal relationship using transfer entropy. And then through optimization, it reduced the model biases on both prediction error and structure difference between model captured variable dependency and observation-based causal strength. Below, we introduce the weight assignment mechanism (attention mechanism) in the LSTM approach and describe details of how we incorporate causality constraints in the model.

Similar to the baseline LSTM, the  $i$ th driving variable at time step  $t$  can be iteratively transformed to a hidden state vector  $h_t^i$  through the gate mechanism (Guo et al., 2019a; Hochreiter and Schmidhuber, 1997; Li et al., 2020; Li et al., 2017). To represent the importance of the  $i$ th variable at time step  $t$ , a weight,  $w_t^i$  or  $w_t^i$ , is dynamically calculated through Eqs (4) and (5), and assigned to  $h_t^i$ . Then, the weighted summation  $h_{sum}^i$  of  $h_t^i$  across time steps is obtained to represent the summarized information for the  $i$ th driving variable.

$$w_t^i = \tanh(W_p h_t^i) \quad (4)$$

$$w_t^i = \frac{e^{w_t^i}}{\sum_{t_0=1}^T e^{w_{t_0}^i}} \quad (5)$$

$$h_{sum}^i = \sum_{t=1}^T w_t^i h_t^i \quad (6)$$

Where  $W_p$  is a parameter matrix that needs to be learned, and  $\tanh$  is the hyperbolic tangent function.  $T$  is the total number of time steps.

To further represent the relative importance of the  $i$ th driving variable compared to other driving variables, a weight,  $\alpha_i$ , is obtained and normalized as  $\alpha_i'$ :

$$\alpha_i = \tanh(W_a [h_{sum}^i, h_T^i]) \quad (7)$$

$$\alpha_i' = \frac{e^{\alpha_i}}{\sum_{j=1}^n e^{\alpha_j}} \quad (8)$$

where  $W_a$  is a learnable parameter matrix.

Finally, using the weighted sum of all driving variables, the model generates the prediction  $\hat{Y}_{T+1}$ :

$$o_i = W_o [h_{sum}^i, h_T^i] + b_o \quad (9)$$

$$\hat{Y}_{T+1} = \sum_{i=1}^n o_i \alpha_i' \quad (10)$$

where the linear function with weight  $W_o$  and bias  $b_o$ , along with weight  $\alpha_i'$  produce the final prediction.

To make the internal structure of the model more consistent with underlying physical processes, we use transfer entropy inferred causal relationships to constrain the variable importance (variable weight) in the predictive model. A larger transfer entropy from a driver (e.g., soil temperature) to  $F_{CH_4}$  implies variations of the driver can cause larger variations in  $CH_4$  emissions, compared to other drivers (Ruddell and Kumar, 2009). Similarly, a larger variable weight ( $\alpha_i'$ ) indicates that the  $i$ th variable plays more important roles in modeling the target variable (Guo et al., 2019a; Li et al., 2020; Li et al., 2018; Li et al., 2017). To guide the model to learn dependencies between causally dominant drivers and  $F_{CH_4}$ , we measure the difference between transfer entropy inferred feature importance vector  $\alpha_{TE}$  and that of the model captured feature importance vector  $\alpha_k$  for each sample  $k$ , and integrate the difference along with modeled errors into the final loss function (Eq. (11)). In the vector  $\alpha_{TE}$ ,  $\alpha_{TE_i}$  represents the transfer entropy from the  $i$ th driving variable to  $F_{CH_4}$ . In  $\alpha_k$ ,  $\alpha_{k,i}$  represents the  $i$ th variable weight,  $\alpha_{k,i}'$ , for a sample  $k$ . Each vector is divided by its summation to obtain a probability distribution ranging from 0 to 1, and KL-Divergence (Kullback and Leibler, 1951) (the second item in the loss function, Eq. (11)) is used to measure the distribution difference between the two vectors.

$$Loss = \frac{1}{N} \sum_{k=1}^N (\hat{Y}_k - Y_k)^2 + \lambda \sum_{k=1}^N \sum_{i=1}^n \alpha_{TE_i} \left| \log \frac{\alpha_{TE_i}}{\alpha_{k,i}} \right| \quad (11)$$

where  $\lambda$  is a structural punishment parameter, and a larger  $\lambda$  means that the model puts more emphasis on structural similarity instead of errors. In Eq. (11), the first right hand side term is the errors between observations and predictions, while the second term is the structural similarity between causality inferred feature importance and importance the model captured.  $N$  is the number of predicted data samples, and  $n$  is the number of variables. The baseline LSTM uses only the first term on the right-hand side for the loss function, while the causal-LSTM has additional constraint from causal relationships via the second term (Eq. (11)).

The model parameters are learned via a back-propagation algorithm (Rumelhart et al., 1986) by minimizing the integrated loss (Eq. (11)) with a variational dropout to avoid overfitting (Gal and Ghahramani, 2016). We used the intra-site validation scheme to test model performance on capturing intra-site temporal variations of  $F_{CH_4}$ . Specifically, in each experiment, for each site, we randomly sampled 80% of data as a training dataset, remained 10% as a validation dataset (used to avoid overfitting during training (Pechoux, 1998)), and retained the remaining 10% as a test dataset (a holdout dataset used to unbiasedly evaluate the final model). We repeated each experiment 20 times to reduce model bias due to random data selection. We compared the model performance with different  $\lambda$  values (Fig. S2), and selected the best one ( $\lambda = 0.005$ ) that has the lowest prediction errors. To evaluate the lag effects for model improvement, we varied the lengths (one-week vs one-month) of time series input used in the models. In addition, we also used the leave-one-site-out scheme (here referred as inter-site validation) (Jung et al., 2011) to test model performance on spatial extrapolation of  $F_{CH_4}$  on each tested site. Other detailed experimental settings of each model are listed in Table S2.

## 3. Results

### 3.1. Causal relationships derived from transfer entropy

Transfer entropy analysis revealed that daily  $F_{CH_4}$  was most strongly

driven by soil temperature ( $T_s$ ) in the four analyzed wetland ecosystem types (bog, fen, marsh, and wet tundra; Fig 2a), with a range of different time lags. The statistics of dominant drivers at each individual site also showed that  $T_s$  dominated in most sites (Fig. S3). Furthermore, the strength of the  $T_s \rightarrow F_{CH_4}$  relationship declined with increasing mean air temperature (slope = -0.0014, R value = -0.63, pvalue < 0.05) (Fig. 2b). This inverse relationship suggested that  $CH_4$  emissions in colder regions were more sensitive to temperature than in warmer areas. The control from air temperature ( $T_a$ ) was weaker than that from  $T_s$  and was prominent only at fen and marsh wetlands (Fig. 2a).

Two biological factors, Ecosystem Respiration (RECO) and plant Gross Primary Production (GPP), also exerted strong controls on daily  $F_{CH_4}$  in bog, fen, and marsh wetlands. These strong relationships between  $F_{CH_4}$  and vegetation carbon turnover are consistent with the findings of many previous studies (Halala et al., 2012a; Mtra et al., 2020; Rime et al., 2018). Plant GPP stimulates  $CH_4$  production indirectly by providing carbon input, mainly via root exudates fueling microbial activity, which produces substrates (such as acetate and  $CO_2$ ) for acetotrophic and hydrogenotrophic methanogenesis (Bastviken, 2009; Mtra et al., 2020; Ström et al., 2012; Whiting and Charlton, 1993). Additionally, GPP can be seen as a proxy of plant-mediated  $CH_4$  transport via aerenchyma tissue (Bastviken, 2009; King et al., 1998; Turetsky et al., 2014). Previous studies argued that the relationship between GPP and  $F_{CH_4}$  may be due to covariation with confounding drivers (e.g., soil temperature) (Chang et al., 2021; Knox et al., 2019). In this study, we confirmed the existence of a strong coupling from GPP and RECO with  $F_{CH_4}$  by removing confounding effects when identifying the causal relationships across multiple wetland types.

Compared with temperature and biological factors, the controls from other variables on  $F_{CH_4}$  were much weaker (Figs 2a, S3) and less consistent across wetland types. For example, VPD controlled  $F_{CH_4}$  more at bog and fen ecosystems, while PA showed weak causal relationships with  $F_{CH_4}$  across all sites. For water-related factors, significant controls on  $F_{CH_4}$  existed only at a few sites, which may be attributed to limited observations of water table depth ( $D_{wt}$ , 16 sites) and soil water content ( $\theta$ , 9 sites), and limited variations of soil wetness across studied sites (more details are discussed in Section 4.1).

### 3.2 $F_{CH_4}$ predictions with causal constraints

Because causal relationships varied across wetland ecosystems, we trained independent ML models for each wetland type (bog, fen, marsh, and wet tundra). Two types models were considered: Long Short-Term Memory (LSTM) and causality-constrained interpretable LSTM (causal-LSTM). We found that Causal-LSTM performed consistently better than

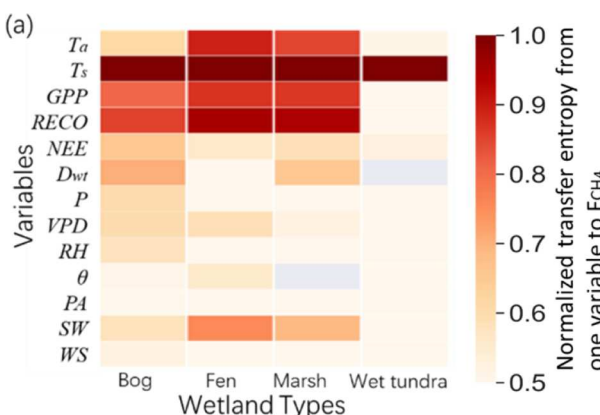


Fig. 2. (a) Causal relationships between environmental and biological factors and daily  $F_{CH_4}$ , averaged across sites within four wetland ecosystems. Colors in the grid squares show the strength of transfer entropy (normalized to range from 0 to 1) from each variable to  $F_{CH_4}$ ; darker colors represent larger values (a grey grid means that the observation data is unavailable). (b) Relationship between the strength of  $T_s \rightarrow F_{CH_4}$  relationships and site Mean Annual Temperature (MAT); the grey bounds show a 95% confidence interval.

LSTM for all four wetland types with higher Pearson correlation coefficient (R) and lower relative MAE (mean absolute error) when inputting four weeks of historical drivers (Table S3 and S4). For example, R values in LSTM ranged from 0.861 to 0.908 and relative MAE ranged from 0.271 to 0.433, while R in causal-LSTM ranged from 0.904 to 0.921 and relative MAE ranged from 0.217 to 0.368 (Fig. 3, Tables S3 and S4). Consistently, with one week of inputs, the causal-LSTM also showed significantly higher R and lower relative MAE compared with LSTM in all wetland types ( $p < 0.05$ , Tables S5 and S6). We also compared the causal-LSTM approach with four other widely used ML algorithms (random forest, decision tree, artificial neural networks, and support vector machine), and found that causal-LSTM had the highest prediction accuracy (Fig. S4), with R value of 0.94 between observations and predictions of causal-LSTM across all sites (Fig. S5).

For model evaluation with the inter-site validation scheme, causal-LSTM also performed reasonably well with R value of 0.75 between observations and predictions (Fig. S6) and lower biases than that of LSTM (Table S7). However, the inter-site validation performance of causal-LSTM dropped, compared with the intra-site validation scheme

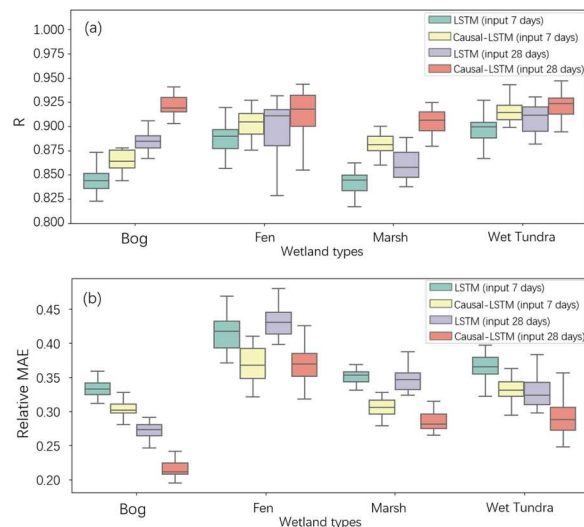
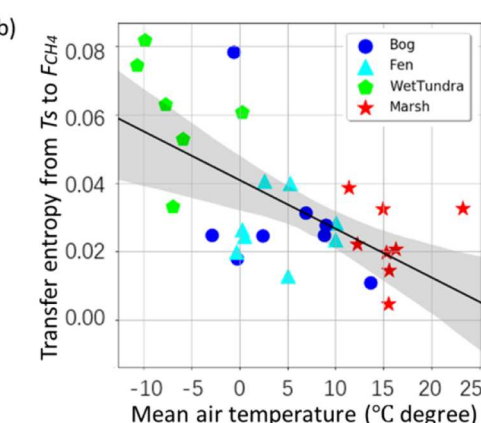


Fig. 3. Model performance comparison with different input lengths for LSTM (green and purple boxes) and causal-LSTM (yellow and red boxes), in terms of (a) correlation coefficient (R), and (b) relative MAE between predictions and observations. The boxes represent 25th to 75th percentiles, and the whiskers represent 5th to 95th percentiles of R or MAE for each wetland type.



especially for the marsh (the mean R value dropped to 0.81 in bog, 0.86 in fen, 0.86 in wet tundra, and 0.69 in marsh), which may be due to the strong spatial heterogeneity of  $F_{CH_4}$  magnitude (e.g., mean  $CH_4$  emission ranged from 2706 nmol  $m^{-2} s^{-1}$  to 165,472 nmol  $m^{-2} s^{-1}$  across different sites) and environmental conditions (e.g., annual precipitation in marsh varied from ~ 200 to ~ 1400 mm/year). Overall, we conclude that the causal-LSTM provides the most effective approach to model wetland  $F_{CH_4}$ .

The results showed that model performance tended to be improved as the length of input time series increased from one to four weeks for both causal-LSTM (Fig. 3a and b, yellow vs red bars) and LSTM models (Fig. 3a and b, green vs purple bars). For R, the performance of both models at bog and marsh was significantly ( $p < 0.05$ ; Tables S8 and S9) improved as the input data length increased. Similarly, in terms of relative MAE, the causal-LSTM model showed significantly lower biases ( $p < 0.05$ ; Table S10) in bog, marsh, and wet tundra ecosystems, and LSTM showed significantly lower biases in bog and wet tundra ( $p < 0.05$ ; Table S11). Overall, longer histories of drivers (i.e., memories) can provide additional information for predictions, especially in bog, marsh, and wet tundra.

#### 4. Discussions

##### 4.1. Soil temperature versus soil water control on $F_{CH_4}$

Wetland  $CH_4$  emissions are regulated by multiple biotic (i.e., production, oxidation) and abiotic (i.e., advection, diffusion) processes, with each posing different dependencies on environmental factors. Therefore, the emergent relationships between wetland methane emissions and the corresponding environmental factors are expected to be complex and diverse across different wetland ecosystem types and across sites with different climate conditions (Turetsky et al., 2014). Among those environmental variables, previous studies have identified temperature and soil water content as major abiotic drivers for wetland  $CH_4$  emissions (Knox et al., 2021; Song et al., 2011; Strachan et al., 2015) because soil water saturation and warm soil conditions are two prerequisites for anaerobic production of wetland  $CH_4$  (Riley et al., 2011).

Here, we found strong soil temperature control on  $CH_4$  emissions across bog, fen, marsh, and wet tundra ecosystems. The stronger causal relationship of  $T_s \rightarrow F_{CH_4}$  compared to  $T_a \rightarrow F_{CH_4}$  is consistent with the hypothesis that air temperature may decouple from soil temperature in colder ecosystems (e.g., wet tundra) due to snow insulation of the ground (Kim et al., 2007). Similar strong correlations between  $T_s$  and wetland  $F_{CH_4}$  have been reported in numerous site-level studies (Granberg et al., 1997; Knox et al., 2021; Mbrin, 2019).

We also found relatively weak control from soil water related variables (Fig. 2), albeit low confidence because of limited data. For example, soil water content had weak control in fen ecosystems, and water table depth had moderate control in bog and marsh ecosystems, but not in fen or wet tundra ecosystems. The lack of sensitivity may partly be due to the data quality of water related variables ( $D_{wt}$  is available in ~ 50% of our studied 30 sites, and  $\theta$  is available in only ~ 30% of the 30 sites (Table S1)). Another potential reason is the fact that the sites used in this study all experienced relatively low variation of  $D_{wt}$  (mean standard deviation is 10.6 cm). Strong seasonal fluctuations of soil water are more expected at rice paddy or tropical swamp ecosystems (Jauhainen et al., 2005; Mezbahuddin et al., 2014), which are not included in this study. For example, water table depth could vary ~ 80 cm at a managed rice paddy site in northern California and plays an important role in driving  $CH_4$  emissions during both growing season and fallow periods (Knox et al., 2016). Although not frequently occurred, extreme droughts may result in significantly different water table at fen and bog sites that will reduce the methane emission (Brown et al., 2014; Rinne et al., 2020). However, ML model was trained with majority of the data to capture non-extreme conditions. In addition, we note that

several studies reported weak dependencies between  $D_{wt}$  and  $F_{CH_4}$  (Jakkowicz-Korczyński et al., 2010; Rinne et al., 2007; Rinne et al., 2018). Given the limitations in sites and water-related data availability, our results highlight the need for more eddy covariance and ancillary measurements in bog, fen, marsh, and wet tundra ecosystems, particularly measurements under long-term drying and rewetting conditions or experiencing natural flooding and water table fluctuation. These observations will facilitate a more complete picture of how various factors affect wetland  $CH_4$  emissions within these wetland ecosystems.

#### 4.2. Causal relationships in model evaluation and development

In addition to commonly used model evaluation metrics (e.g., MAE and R), causal inference provided additional metrics to evaluate and benchmark models in terms of internal causal structures. Causal relationships may also help select process-based models with model causal structures similar to those in observations. In this analysis, we found that methane ML models can achieve comparable performance even though they have diverse causal relationships. We visualized variable importance within LSTM and causal-LSTM models and validated the modeled relationships against observed causal relationships identified by transfer entropy analysis (Fig. 4). The feature importance of causal-LSTM and LSTM were calculated according to attention weight statistics (Guo et al., 2019b; Li et al., 2020) and the feature importance derived from RFE (Guyon et al., 2002; Meyer et al., 2019) of 20 repeated experimental results, respectively, and were both normalized to 0–1. We found that LSTM mainly used dependencies from wind, atmospheric pressure, soil and air temperature, and total ecosystem respiration to estimate  $F_{CH_4}$ , which were different from those inferred from observations and causal-LSTM (Fig. 4). The feature importance in the causal-LSTM model is much more consistent with observations, confirming the effectiveness of the causality constraints.

The inferred causal relationships from biological and environmental variables on  $CH_4$  emissions vary across different wetland types and time windows. Our results show that soil temperature dominantly controls  $F_{CH_4}$  in wet tundra, while biotic variables along with soil temperature co-dominate  $F_{CH_4}$  in fens, bogs, and marshes. The different controls imply that different ecosystems need to be considered separately in machine learning model development (Turetsky et al., 2014). Also for each wetland ecosystem, the responses of  $F_{CH_4}$  rely on processes with short time lags (e.g.,  $CH_4$  transport, microbial activity) and long time lags (e.g., fine root turnover). Integrating both short and long causal relationships may also improve model performance.

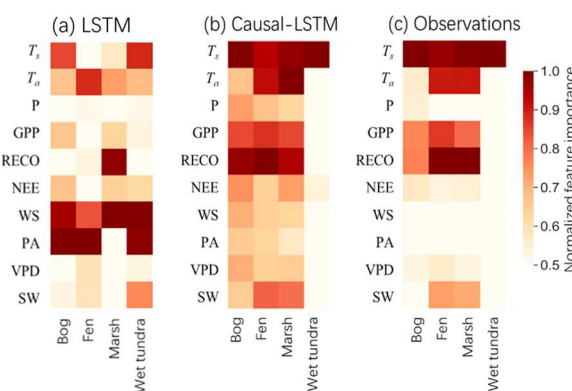


Fig. 4. Comparison of feature importance in (a) LSTM, (b) causal-LSTM, and (c) observations. Colors show the corresponding normalized feature importance that is normalized between 0 and 1, with higher value indicating higher importance.

#### 4.3 Implications of considering causal relationships in $\text{CH}_4$ emission projections

Our results, in line with previous studies, suggest that data-driven ML models may accurately reproduce observations with the wrong reasons (Pearl, 2019; Reichstein et al., 2019; Runge et al., 2019). The different causal relationships built within predictive models are critically important for climate change projections, since the responses of  $\text{CH}_4$  emissions to climate change strongly depend on the strength of the underlying causal relationships. Thus we hypothesized that although both LSTM and causal-LSTM performed reasonably well under present-day conditions, their predictions under warming climate could differ due to their differences in internal functional relationships or altered combinations of forcing mechanisms. To test this hypothesis, we conducted a theoretical soil warming experiment ( $+1^\circ\text{C}$ ) at all sites through modeling. We acknowledged that more complex changes can occur in a real soil warming experiment (e.g., soil drying caused by warming) (Pries et al., 2017). However, this simple soil warming experiment isolates impacts from other environmental or biological variables and focuses only on the temperature effect.

For each wetland type, we calculated the mean change in  $\text{FCH}_4$  due to soil warming across all site years. We defined response ratio to warming by percentage change of  $\text{FCH}_4$  under warmed and controlled conditions. Large differences between the LSTM and causal-LSTM existed in response to warming, especially for bogs (4% vs 21.8%) and fens (27% vs 101%) (Fig. 5). The differences in causal-LSTM predictions are significantly larger than those of LSTM for bog, fen, marsh and wet tundra sites ( $p < 0.05$ ; Table S12). Overall, the LSTM model estimated lower methane emission in response to warming than causal-LSTM model, primarily due to the less important role of soil temperature in its internal model functions (Fig. 4a). Therefore, this work highlights the importance of considering causal relationships in modeling  $\text{CH}_4$  emissions under a changing climate. We advocate the use of these types of causal relationship constraints for other ecosystem variables calculated through machine learning approaches (e.g., FLUXNET-MTE GPP (Jung et al., 2011)). In addition, causality constrained ML models could serve as surrogate modules for efficient parameterization and high accuracy prediction, especially for processes that lack theoretical understanding and mathematical model structures.

#### 5. Conclusions

Based on in situ eddy covariance measurements of daily  $\text{CH}_4$  emissions ( $\text{FCH}_4$ ) at 30 eddy covariance sites in bog, fen, marsh, and wet tundra wetlands, we found consistent causal regulations from soil temperature on  $\text{FCH}_4$  using a transfer entropy approach. We also confirmed important causal relationships with ecosystem respiration (RECO) and gross primary production at bog, fen, and marsh wetlands. The transfer entropy approach explicitly excludes confounding variables and therefore reduces the possibility that the observed causal relationship between  $\text{FCH}_4$  and RECO or GPP was due to covariation with other environmental drivers, such as temperature (Chu et al., 2014; Knox et al., 2019). We then developed a predictive model that integrated the transfer entropy inferred causal relationships for  $\text{FCH}_4$  simulations. The causality constrained model outperformed other baseline ML models in terms of accuracy (relative MAE and R); more importantly, we demonstrated that including underlying causal relationships in predicting  $\text{FCH}_4$  under a  $1^\circ\text{C}$  soil warming could differ by up to a factor of 4, compared with traditional ML models. Our results highlighted that those causal relationships can be used to benchmark, evaluate, and improve wetland methane emission models. Our proposed causality constrained model could benefit large-scale upscaling, data gap filling, and surrogate modeling of wetland  $\text{CH}_4$  emissions within earth system land models.

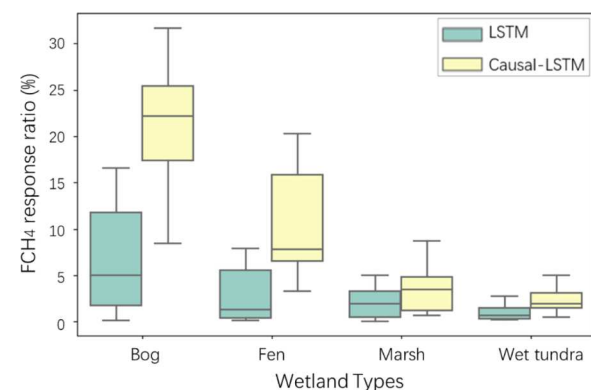


Fig. 5.  $\text{FCH}_4$  response ratio to an imposed  $+1^\circ\text{C}$  soil warming of LSTM (green) and causal-LSTM (yellow) models. The boxes represent 25th to 75th percentiles and the whiskers represent 5th to 95th percentiles of R or MAE for each wetland type.

#### Declaration of Competing Interest

The authors declare that they have no known competing financial interests or personal relationships that could be perceived to influence the work reported in this paper.

#### Data availability

Data will be made available on request.

#### Acknowledgments

This research was primarily supported by NASA Carbon Monitoring System grant (#NNH20ZDA001N) and the Reducing Uncertainties in Biogeochemical Interactions through Synthesis and Computation (RUEISOC) Scientific Focus Area Project, the latter is sponsored by the Earth and Environmental Systems Modeling (EESM) Program under the Office of Biological and Environmental Research of the US Department of Energy Office of Science. Min Chen acknowledges the support from NASA Terrestrial Ecology Arctic Boreal Vulnerability Experiment Phase 2 program (#SONSSC21K1702). Margaret Torn acknowledges the support from The Next-Generation Ecosystem Experiments (NGEE Arctic) project under the Office of Biological and Environmental Research in the DOE Office of Science. We acknowledge support from John Wesley Powell Center for Analysis and Synthesis of the U.S. Geological Survey ('Wetland FLUXNET Synthesis for Methane' working group). Any use of trade, firm or product names is for descriptive purposes only and does not imply endorsement by the U.S. Government.

#### Supplementary materials

Supplementary material associated with this article can be found, in the online version, at [doi:10.1016/j.agrformet.2022.109115](https://doi.org/10.1016/j.agrformet.2022.109115).

#### References

- Abdul Razak, F., Jensen, H.J., 2014. Quantifying 'causality' in complex systems using transfer entropy. *PLoS One* 9 (6), e99462.
- Alahi, A., et al., 2016. Social Istm: Human trajectory prediction in crowded spaces. In: *Proceedings of the IEEE conference on computer vision and pattern recognition*, pp. 961–971.
- Basilevsky, D., 2009. Methane.
- Bergamaschi, P., et al., 2013. Atmospheric  $\text{CH}_4$  in the first decade of the 21st century: inverse modeling analysis using SCIAVCHY satellite retrievals and NOAA surface measurements. *J. Geophys. Res. Atmos.* 118 (13), 7360–7369.
- Bergman, I., Klarqvist, M., Nilsson, M., 2000. Seasonal variation in rates of methane production from peat of various botanical origins: effects of temperature and substrate quality. *FEEMS Microbiol. Ecol.* 33 (3), 181–189.

Bohrer, G. and Mbrin, T.H., 2020. FLUXNET-CH4 US-ORv Clentangy River Wetland Research Park, United States

Boothroyd, I.M., Almond, S., Worrall, F., Davies, R., 2017. Assessing the fugitive emission of CH<sub>4</sub> via migration along fault zones: comparing potential shale gas basins to non-shale basins in the UK. *Sci. Total Environ.* 580, 412–424.

Bouskill, N.J., Riley, W.J., Zhu, Q., Mekonnen, Z.A., Grant, R.F., 2020. Alaskan carbon-climate feedbacks will be weaker than inferred from short-term experiments. *Nat. Commun.* 11 (1), 1–12.

Bousquet, P., et al., 2006. Contribution of anthropogenic and natural sources to atmospheric methane variability. *Nature* 443 (7110), 439–443.

Brown, M.G., Humphreys, E.R., Moore, T.R., Roulet, N.T., Lafleur, P.M., 2014. Evidence for a nonmonotonic relationship between ecosystem-scale peatland methane emissions and water table depth. *J. Geophys. Res. Biogeosci.* 119 (5), 826–835.

Campbell, D., Goodrich, J., 2020. FLUXNET-CH4 NZ-Kop Koputai, New Zealand.

Castro-Morales, K., et al., 2018. Year-round simulated methane emissions from a permafrost ecosystem in Northeast Siberia. *Biogeosciences* 15 (9), 2691–2722.

Chadburn, S.E., et al., 2020. Modeled microbial dynamics explain the apparent temperature sensitivity of wetland methane emissions. *Global Biogeochem Cycles* 34 (11), e2020GB006768.

Cheng, K.-Y., Riley, W.J., Orill, P.M., Grant, R.F., Saleska, S.R., 2020. Hysteretic temperature sensitivity of wetland CH<sub>4</sub> fluxes explained by substrate availability and microbial activity. *Biogeosciences* 17 (22), 5849–5860.

Cheng, K.-Y., et al., 2021. Substantial hysteresis in emergent temperature sensitivity of global wetland CH<sub>4</sub> emissions. *Nat. Commun.* 12 (1), 1–10.

Cheng, K.Y., et al., 2019. Methane production pathway regulated proximally by substrate availability and distally by temperature in a high-latitude mire complex. *J. Geophys. Res. Biogeosci.* 124 (10), 3057–3074.

Chen, H., Xu, X., Fang, C., Li, B., Nie, M., 2021. Differences in the temperature dependence of wetland CO<sub>2</sub> and CH<sub>4</sub> emissions vary with water table depth. *Nat. Clim. Change* 11 (9), 766–771.

Chen, J. and Chu, H., 2020. FLUXNET-CH4 US-WPT Winooski Point North Marsh, United States

Chen, Y.H., Prinn, R.G., 2006. Estimation of atmospheric methane emissions between 1996 and 2001 using a three-dimensional global chemical transport model. *J. Geophys. Res. Atmos.* 111 (D10).

Chu, H., et al., 2014. Net ecosystem methane and carbon dioxide exchanges in a Lake Erie coastal marsh and a nearby cropland. *J. Geophys. Res. Biogeosci.* 119 (9), 722–740.

Dean, J.F., et al., 2018. Methane feedbacks to the global climate system in a warmer world. *Rev. Geophys.* 56 (1), 207–250.

Delwiche, K.B., et al., 2021. FLUXNET-CH4 a global, multi-ecosystem dataset and analysis of methane seasonality from freshwater wetlands. *Earth Syst. Sci. Data* 13 (7), 3607–3689.

Desai, A.R. and Thom, J., 2020. FLUXNET-CH4 US-Los Lios Creek, United States

Eichelman, E., et al., 2020. FLUXNET-CH4 US-Tw4 Twitchell East End Wetland, United States

Euskirchen, E., Bret-Harte, M. and Edgar, C., 2020. FLUXNET-CH4 US-Ios Inuvavik Creek Watershed Wet Sedge Tundra, United States

Euskirchen, E. and Edgar, C., 2020a. FLUXNET-CH4 US-BZB Bonanza Creek Thermokarst Bog, United States

Euskirchen, E. and Edgar, C., 2020b. FLUXNET-CH4 US-BZF Bonanza Creek Rich Fen, United States

Fan, L., et al., 2021. A divergent metabolic pathways of anaerobic methane oxidation in paddy soils. *Sci. Biol. Biochem.* 156, 10215.

Gal, Y., Ghahramani, Z., 2016. A theoretically grounded application of dropout in recurrent neural networks. *Adv. Neural Inf. Process. Syst.* 29, 1019–1027.

Göckede, M., 2020. FLUXNET-CH4 RU-Ch2 Chersky reference, Russia

Göckede, M., et al., 2019. Negative feedback processes following drainage slow down permafrost degradation. *Global Change Biol.* 25 (10), 3254–3266.

Goodrich, J., Campbell, D., Roulet, N., Clearwater, M., Schipper, L., 2015. Overriding control of methane flux temporal variability by water table dynamics in a Southern Hemisphere raised bog. *J. Geophys. Res. Biogeosci.* 120 (9), 819–831.

Granberg, G., Mikkola, C., Sundh, I., Svensson, B.H., Nilsson, M., 1997. Sources of spatial variation in methane emission from mires in northern Sweden: a mechanistic approach in statistical modeling. *Global Biogeochem Cycles* 11 (2), 135–150.

Grant, R., Humphreys, E., Lafleur, P., 2015. Ecosystem CO<sub>2</sub> and CH<sub>4</sub> exchange in a mixed tundra and a fen within a hydrologically diverse Arctic landscape. 1. Modeling versus measurements. *J. Geophys. Res. Biogeosci.* 120 (7), 1366–1387.

Grant, R., Mekonnen, Z., Riley, W., Arora, B., Torn, M., 2017a. 2. Morphotopography determines how CO<sub>2</sub> and CH<sub>4</sub> exchange responds to changes in temperature and precipitation at an Arctic polygonal tundra site. Mathematical modelling with Ecosys. *J. Geophys. Res. Biogeosci.* 122, 3161–3173.

Grant, R., et al., 2017b. I: Morphotopography determines how active layer depths respond to changes in temperature and precipitation at an Arctic polygonal tundra site. Mathematical modelling with Ecosys. *J. Geophys. Res. Biogeosci.* 122, 3161–3173.

Guo, T., Lin, T., Antulov-Fantulin, N., 2019a. Exploring interpretable Istm neural networks over multi-variable data. In: International Conference on Machine Learning. PMLR, pp. 2494–2504.

Guo, T., Lin, T., Antulov-Fantulin, N., 2019b. Exploring interpretable Istm neural networks over multi-variable data. arXiv preprint arXiv:1905.12034.

Guyon, I., Weston, J., Barnhill, S., Vapnik, V., 2002. Gene selection for cancer classification using support vector machines. *Mach. Learn.* 46 (1), 39–422.

Hatala, J.A., Dettlof, M., Baldocchi, D.D., 2012a. Gross ecosystem photosynthesis causes a diurnal pattern in methane emission from rice. *Geophys. Res. Lett.* 39 (9), L06409.

Hatala, J.A., et al., 2012b. Greenhouse gas (CO<sub>2</sub>, CH<sub>4</sub>, H<sub>2</sub>O) fluxes from drained and flooded agricultural peatlands in the Sacramento-San Joaquin Delta. *Agricul. Ecosyst. Environ.* 150, 1–18.

Herres, K.S., Chamberlain, S.D., Eichelman, E., Knox, S.H., Baldocchi, D.D., 2018. A biogeochemical compromise: the high methane cost of sequestering carbon in restored wetlands. *Geophys. Res. Lett.* 45 (12), 6081–6091.

Hinkle, C.R. and Bracho, R., 2020. FLUXNET-CH4 US-DPW Disney Wilderness Preserve Wetland, United States

Hodreiter, S., Schmidhuber, J., 1997. Long short-term memory. *Neural Comput.* 9 (8), 1735–1780.

Holmgren, G.O., et al., 2020. FLUXNET-CH4 US-LA2 Salvador WMA Freshwater Marsh, United States

IPCC, 2013. Chapter 6 carbon and other biogeochemical cycles Climate Change 2013 The Physical Science Basis. Cambridge University Press, Cambridge.

Irvin, J., et al., 2021. Gap-filling eddy covariance methane fluxes: comparison of machine learning model predictions and uncertainties at FLUXNET-CH4 wetlands. *Agric. For. Meteorol.* 308, 108528.

Iwata, H., Ueyama, M. and Harazono, Y., 2020. FLUXNET-CH4 US-Uaf University of Alaska, Fairbanks, United States

Jakowicz-Korczyński, M., et al., 2010. Annual cycle of methane emission from a subarctic peatland. *J. Geophys. Res. Biogeosci.* 115 (G2).

Jansen, J., Friberg, T., Jannet, M. and Orill, P., 2020. FLUXNET-CH4 SE-St1 Stordalen grassland, Sweden

Jauhainen, J., Takahashi, H., Heikkilä, J.E., Martikainen, P.J., Vasander, H., 2005. Carbon fluxes from a tropical peat swamp forest floor. *Global Change Biol.* 11 (10), 1788–1797.

Jung, M., et al., 2011. Global patterns of land-atmosphere fluxes of carbon dioxide, latent heat, and sensible heat derived from eddy covariance, satellite, and meteorological observations. *J. Geophys. Res. Biogeosci.* 116 (G3).

Kantz, H., Schümann, T., 1996. Enlarged scaling ranges for the KS-entropy and the information dimension. *Chaos Interdiscip. J. Nonlinear Sci.* 6 (2), 167–171.

Kim, Y., et al., 2020. Gap-filling approaches for eddy covariance methane fluxes: a comparison of three machine learning algorithms and a traditional method with principal component analysis. *Global Change Biol.* 26 (3), 1499–1518.

Kim, Y., et al., 2007. Assessment of winter fluxes of CO<sub>2</sub> and CH<sub>4</sub> in boreal forest soils of central Alaska estimated by the profile method and the chamber method: a diagnosis of methane emission and implications for the regional carbon budget. *Tellus B Chem. Phys. Meteorol.* 59 (2), 223–233.

King, J.Y., Reeburgh, W.S., Regal, S.K., 1998. Methane emission and transport by arctic sedges in Alaska: results of a vegetation removal experiment. *J. Geophys. Res. Atmos.* 103 (D22), 29083–29092.

Knox, S.H., et al., 2021. Identifying dominant environmental predictors of freshwater wetland methane fluxes across diurnal to seasonal time scales. *Global Change Biol.* 27 (15), 3582–3604.

Knox, S.H., et al., 2019. FLUXNET-CH4 synthesis activity: objectives, observations and future directions. *Bull. Am. Meteorol. Soc.* 100 (12), 2607–2632.

Knox, S.H., et al., 2016. Biophysical controls on interannual variability in ecosystem-scale CO<sub>2</sub> and CH<sub>4</sub> exchange in a California rice paddy. *J. Geophys. Res. Biogeosci.* 121 (3), 978–1001.

Koch, S., Jurasinski, G., Koebisch, F., Koch, M., Glatzel, S., 2014. Spatial variability of annual estimates of methane emissions in a *Phragmites australis* (Cav.) Trin. ex Steud. dominated restored coastal brackish fen. *Wetlands* 34 (3), 593–602.

Koebisch, F. and Jurasinski, G., 2020. FLUXNET-CH4 DE-Hte Huetmoor, Germany.

Koff, E.N., Bergamashi, P., Alkama, R., Cescatti, A., 2020. An observation-constrained assessment of the climate sensitivity and future trajectories of wetland methane emissions. *Sci. Adv.* 6 (15).

Kullback, S., Leibler, R.A., 1951. On information and sufficiency. *Ann. Math. Stat.* 22 (1), 79–86.

Li, F., et al., 2020. A hierarchical temporal attention-based LSTM encoder-decoder model for individual mobility prediction. *Neurocomputing*.

Li, F., Zhu, Q., Riley, W.J., Yuan, K., Wu, H., Gui, Z., 2022. Wetter California projected by CMIP6 models with observational constraints under a high GHG emission scenario. *Earth's Future* 10 (4) e2022EF002694.

Liang, Y., Ke, S., Zhang, J., Yi, X., Zheng, Y., 2018. Geomat: multi-level attention networks for geo-sensor time series prediction. *IJCAI* 3428–3434.

Liu, B.Y., et al., 2019. Using information theory to evaluate directional precipitation interactions over the West Sahel region in observations and models. *J. Geophys. Res. Atmos.* 124 (3), 1463–1473.

Lohila, A., et al., 2020. FLUXNET-CH4 FI-Lam Larpaljärvi, Finland.

Matthes, J.H., et al., 2020. FLUXNET-CH4 US-Mjb Mayberry Wetland, United States

Mayer, H.P., Conrad, R., 1990. Factors influencing the population of methanogenic bacteria and the initiation of methane production upon flooding of paddy soil. *FEBS Microbiol. Ecol.* 6 (2), 103–111.

Melton, J.R., et al., 2013. Present state of global wetland extent and wetland methane modelling conclusions from a model inter-comparison project (WETCHIMP). *Biogeosciences* 10 (2), 753–788.

Meyer, H., Reudenbach, C., Wöllauer, S., Naus, T., 2019. Importance of spatial predictor variable selection in machine learning applications: moving from data reproduction to spatial prediction. *Ecol. Model.* 411, 108815.

Mebahuddin, M., Grant, R.F., Hirano, T., 2014. Modelling effects of seasonal variation in water table depth on net ecosystem CO<sub>2</sub> exchange of a tropical peatland. *Biogeosciences* 11 (3), 577–599.

Mitra, B., et al., 2020. Spectral evidence for substrate availability rather than environmental control of methane emissions from coastal forested wetland. *Agric. For. Meteorol.* 291, 108062.

Mbraffah, R., Kararri, M., Guo, R., Raglin, A., Liu, H., 2020. Causal interpretability for machine learning problems: methods and evaluation. *ACM SIGKDD Explorations Newsletter* 22 (1), 18–33.

Morin, T., et al., 2014. Environmental drivers of methane fluxes from an urban temperate wetland park. *J. Geophys. Res. Biogeosci.* 119 (11), 2188–2208.

Morin, T.H., 2019. Advances in the eddy covariance approach to  $\text{CH}_4$  monitoring over two and a half decades. *J. Geophys. Res. Biogeosci.* 124 (3), 453–460.

Nilsson, M.B. and Reich, M., 2020. FLUXNET-CH4 SE-Deg Degerö, Sweden.

Oertel, C., Mätschallat, J., Zurba, K., Zirmann, F., Erasmi, S., 2016. Greenhouse gas emissions from soils – a review. *Geochemistry* 76 (3), 327–352.

Pasut, C., Tang, F.H., Hamilton, D., Riley, W.J., Maggi, F., 2021. Spatiotemporal assessment of GHG emissions and nutrient sequestration linked to Agro-nutrient runoff in global wetlands. *Global Biogeochem. Cycles* 35 (4), e2020GB006816.

Pearl, J., 2019. The limitations of opaque learning machines. *Possible Minds Twenty-Five Ways of Looking at AI*, pp. 13–19.

Petralia, O., et al., 2019. Monthly gridded data product of northern wetland methane emissions based on upscaling eddy covariance observations. *Earth Syst. Sci. Data* 11 (3), 1263–1289.

Predtak, L., 1998. Early stopping but when? neural networks tricks of the trade, lecture notes in computer science. Springer, Heidelberg, p. 1524.

Pries, C.E.H., Castanha, C., Porrà, R., Tom, M., 2017. The whole soil carbon flux in response to warming. *Science* 355 (6332), 1420–1423.

Qin, Y., et al., 2017. A dual-stage attention-based recurrent neural network for time series prediction. *arXiv preprint arXiv:1704.02971*.

Reichstein, M., et al., 2019. Deep learning and process understanding for data-driven Earth system science. *Nature* 566 (7749), 195–204.

Rey-Sánchez, A., Morin, T., Stefanik, K., Wrighton, K., Bohrer, G., 2018. Determining total emissions and environmental drivers of methane flux in a Lake Erie estuarine marsh. *Ecol. Eng.* 114, 7–15.

Riley, W., et al., 2011. Barriers to predicting changes in global terrestrial methane fluxes analyses using CLIVM $\delta$ , a methane biogeochemistry model integrated in CESM. *Biogeosciences* 8 (7), 1925–1953.

Rinne, J., et al., 2007. Annual cycle of methane emission from a boreal fen measured by the eddy covariance technique. *Tellus B: Chem. Phys. Meteorol.* 59 (3), 449–457.

Rinne, J., et al., 2018. Temporal variation of ecosystem scale methane emission from a boreal fen in relation to temperature, water table position, and carbon dioxide fluxes. *Global Biogeochem. Cycles* 32 (7), 1087–1105.

Rinne, J., et al., 2020. Effect of the 2018 European drought on methane and carbon dioxide exchange of northern mire ecosystems. *Philos. Trans. R. Soc. B* 375 (1810), 20190517.

Ruddell, B.L., Kurar, P., 2009. Ecosystem process networks: 1. Identification. *Water Resour. Res.* 45 (3).

Rumelhart, D.E., Hinton, G.E., Williams, R.J., 1986. Learning representations by back-propagating errors. *Nature* 323 (6088), 533–536.

Runge, J., et al., 2019a. Inferring causation from time series in Earth system sciences. *Nat. Commun.* 10 (1), 1–13.

Runge, J., Nonnaker, P., Kretschmer, M., Flaxman, S., Sejdinovic, D., 2019b. Detecting and quantifying causal associations in large nonlinear time series datasets. *Sci. Adv.* 5 (11), eaau4996.

Sachs, T. and Wille, C., 2020. FLUXNET-CH4 DE-Zirk Zamekow, Germany.

Saunois, M., et al., 2020. The global methane budget 2000–2017. *Earth Syst. Sci. Data* 12 (3), 1561–1623.

Schaufel, G., et al., 2010. Greenhouse gas emissions from European soils under different land use: effects of soil moisture and temperature. *Eur. J. Soil Sci.* 61 (9), 683–696.

Schmid, H.P. and Klett, J., 2020. FLUXNET-CH4 DE-SIN Schechenf Iz Nord, Germany.

Schreiber, T., 2000. Measuring information transfer. *Phys. Rev. Lett.* 85 (2), 461.

Schuur, E.A., et al., 2008. Vulnerability of permafrost carbon to climate change: implications for the global carbon cycle. *Bioscience* 58 (8), 701–714.

Short, R., Herremans, K., Szutu, D., Verfaillie, J., and Baldocchi, D., 2020. FLUXNET-CH4 US-SNE Sherman Island Restored Wetland, United States.

Song, C., Sun, L., Huang, Y., Wang, Y., Wan, Z., 2011. Carbon exchange in a freshwater marsh in the Sanjiang Plain, northeastern China. *Agric. For. Meteorol.* 151 (8), 1131–1138.

Sonnentag, O. and Helbig, M., 2020a. FLUXNET-CH4 CA-SOB Scotty Creek Bog, Canada.

Sonnentag, O. and Helbig, M., 2020b. FLUXNET-CH4 CA-SOB Scotty Creek Landscape, Canada.

Spirits, P., Glymour, C.N., Scheines, R., Heckerman, D., 2000. *Causation, prediction, and search*. MIT press.

Strachan, I.B., Nugent, K.A., Cronbie, S., Bonneville, M.C., 2015. Carbon dioxide and methane exchange at a cool-temperate freshwater marsh. *Environ. Res. Lett.* 10 (6), 065006.

Ström, L., Tagesson, T., Mästepanov, M., Christensen, T.R., 2012. Presence of *Eriophorum scheuchzeri* enhances substrate availability and methane emission in an Arctic wetland. *Soil Biol. Biochem.* 45, 61–70.

Sturtevant, C., et al., 2016. Identifying scale-emergent, nonlinear, asynchronous processes of wetland methane exchange. *J. Geophys. Res. Biogeosci.* 121 (1), 188–204.

Tao, J., Zhu, Q., Riley, W.J., Neumann, R.B., 2020. Improved ELM/1-ECA simulations of zero-curtain periods and cold-season  $\text{CH}_4$  and  $\text{CO}_2$  emissions at Alaskan Arctic Tundra Sites. *Oryosphere Discuss.* 1–48.

Tom, M. and Dengel, S., 2020. FLUXNET-CH4 US-NGB NGB Arctic Barrow, United States.

Turetsky, M.R., et al., 2014. A synthesis of methane emissions from 71 northern, temperate, and subtropical wetlands. *Global Change Biol.* 20 (7), 2183–2197.

Turner, J., Desai, A.R., Thom, J., Wiklund, K., 2021. Lagged wetland  $\text{CH}_4$  flux response in a historically wet year. *J. Geophys. Res. Biogeosci.* 126 (11), e2021JG006458.

Ueyama, M., Hirano, T., and Kominami, Y., 2020. FLUXNET-CH4 JP-BBY Ebai bog, Japan.

Valach, A.C. et al., 2020. FLUXNET-CH4 US-Twi Twitchell Wetland West Pond, United States.

Vaswani, A., et al., 2017. Attention is all you need. *Adv. Neural Inf. Process. Syst.* 5998–6008.

Vesala, T., Tuittila, E.-S., Mammarella, I., and Alekseychik, P., 2020a. FLUXNET-CH4 FI-SI2 Siikaneva-2 Bog, Finland.

Vesala, T., Tuittila, E.-S., Mammarella, I., and Rinne, J., 2020b. FLUXNET-CH4 FI-SI Siikaneva, Finland.

Villa, J.A., et al., 2020. Plant-mediated methane transport in emergent and floating-leaved species of a temperate freshwater mineral-soil wetland. *Limnol. Oceanogr.* 65 (7), 1635–1650.

Villa, J.A., et al., 2021. Ebulition dominates methane fluxes from the water surface across different hydrological patches in a temperate freshwater marsh at the end of the growing season. *Sci. Total Environ.* 767, 144498.

Wählen, M., 1993. The global methane cycle. *Annu. Rev. Earth Planet. Sci.* 21 (1), 407–426.

Wania, R., et al., 2013. Present state of global wetland extent and wetland methane modelling methodology of a model inter-comparison project (WETCHIMP). *Geoscientific Model Dev.* 6 (3), 617–641.

Whalen, S., 2005. Biogeochemistry of methane exchange between natural wetlands and the atmosphere. *Environ. Eng. Sci.* 22 (1), 73–94.

Whiting, G.J., Chanton, J.P., 1993. Primary production control of methane emission from wetlands. *Nature* 364 (6440), 794–795.

Xu, X., et al., 2016. Reviews and syntheses four decades of modeling methane cycling in terrestrial ecosystems. *Biogeosciences* 13 (12), 3735–3755.

Yuan, K., et al., 2021. Deforestation reshapes land-surface energy-flux partitioning. *Environ. Res. Lett.* 16 (2), 024014.

Yuan, K., Zhu, Q., Riley, W.J., Li, F., Wu, H., 2022. Understanding and reducing the uncertainties of land surface energy flux partitioning within CMIP6 land models. *Agric. For. Meteorol.* 319, 108920.

Yvon-Durocher, G., et al., 2014. Methane fluxes show consistent temperature dependence across microbial to ecosystem scales. *Nature* 507 (7493), 488–491.

Zhang, Z., et al., 2017. Emerging role of wetland methane emissions in driving 21st century climate change. *Proc. Natl. Acad. Sci.* 114 (36), 9647–9652.

Zona, D., et al., 2016. Cold season emissions dominate the Arctic tundra methane budget. *Proc. Natl. Acad. Sci.* 113 (1), 40–45.

Zona, D. and Oechel, W.C., 2020a. FLUXNET-CH4 US-Bea Barrow Environmental Observatory (EO) tower, United States.

Zona, D. and Oechel, W.C., 2020b. FLUXNET-CH4 US-Bes Barrow Bes (Biosocomplexity Experiment South tower), United States.

Zona, D. and Oechel, W.C., 2020c. FLUXNET-CH4 US-Ivo Ivotuk, United States.